

Supporting Information for

**Photoluminescence Enhancement of Mn⁴⁺-doped Rb₂NaAlF₆
Single-Crystal Phosphors *via* Heterovalent Co-doping for Wide
Gamut Displays**

Zhen Chen,^a Chuang Zhang,^{a,b} Yuanjing Wang,^{a,b*} Hong Ming,^a Yayun Zhou,^c Enhai Song,^{a*} and

Qinyuan Zhang^{a,b*}

Z. Chen, C. Zhang, Y. J. Wang, Dr. H. Ming, Prof. E. H. Song, Prof. Q.Y. Zhang

^a State Key Laboratory of Luminescent Materials and Devices, South China University of
Technology, Guangzhou 510641, China

Y. Y. Zhou

^b Guangdong-Hong Kong-Macao Joint Laboratory for Intelligent Micro-Nano Optoelectronic
Technology, School of Physics and Optoelectronic Engineering, Foshan University, Foshan
528225, China

Y. J. Wang, C. Zhang, Q. Y. Zhang

^c School of Physics and Optoelectronics, South China University of Technology, Guangzhou
510641, China

*Corresponding E-mail: 441349346@qq.com (Yuanjing Wang), msehsong@scut.edu.cn (Enhai
Song), qyzhang@scut.edu.cn (Qinyuan Zhang)

1. Characterizations

A Bruker SMART APEX IV 4K CCD diffractometer with Mo $K\alpha$ radiation ($\lambda = 0.71073 \text{ \AA}$) was used to collect the single-crystal X-ray diffraction (XRD) data at 296(2) K, and the data were integrated through a SAINT program.¹ The structure was solved with the direct methods and refined with the aid of SHELXTL package.² Powder XRD data for phase purity analysis were collected at RT on a powder X-ray diffractometer (PANalytical AERIS, Cu- $K\alpha$ radiation). The step size of 2θ was 0.011° , and the counting time was 2s per step. X-ray photoelectron spectroscopy (XPS) spectra were recorded by a Thermo Scientific ESCALAB 250Xi electron spectrometer. The morphology and elemental compositions of the samples were detected using a scanning electron microscope (SEM, NOVANANOSEM430) equipped with an attached energy-dispersive X-ray spectrometer (EDS). Photoluminescence excitation (PLE), PL spectra, decay curves, and quantum efficiency (QE) were measured at RT by an Edinburgh fluorescence spectrometer (FLS1000), and a microsecond flash lamp or a 450 W xenon lamp was used as the light source. QE test was performed by using a barium sulfate-coated integrating sphere (150 mm in diameter) that was attached to FLS1000. The temperature dependence PL properties were conducted by the same spectrophotometer with the help of a coupled temperature-controlled cylinder (25-200 °C, TAP-02, Tianjin Orient-KOJI Instrument, China) and a liquid-nitrogen cooling cryostat (77-300 K, TC202, Tianjin Orient-KOJI Instrument, China). Compositional analyses of samples were determined by using an ICP-OES (Agilent Varian 720). The photoelectric properties of the as-fabricated white light-emitting diode (LED) were collected by an ATA-1000 optoelectronic analyzer. The images and videos are recorded by a digital camera (Canon EOS 80D, f/4, 50 fps, ISO-400).

2. w-LED Fabrications for Projector

The w-LEDs were fabricated with blue InGaN chips, β -Sialon green phosphor, red-emitting KSFM, RNAFM-P, RNAFM-C, and RNAFMM-C phosphors. Firstly, red phosphor and commercial β -Sialon green phosphor were mixed thoroughly with ultraviolet epoxy resin to form stable slurry, respectively. Then, the mixture was

adjusted to the appropriate ratio and evenly applied onto the LED chips. A new modified projector was then assembled by using the w-LED (RNAFMM-C phosphor + β -Sialon phosphor) instead of the original backlight source. The projected images are recorded by a digital camera (Canon EOS 80D, f/4, 50 fps, ISO-400).

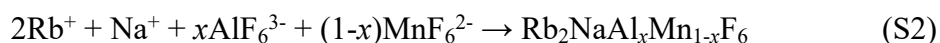
3. Computational Details

Simulations of geometric and electronic structures were performed using the DFT and the generalized gradient approximation based Perdew-Burke-Ernzerhof (PBE) exchange-correlation functional in the Mede A-VASP package.^{3,4} The Na ($3s^1$), Al ($2s^22p^3$), F ($2s^22p^5$), Rb ($5s^1$), Mg ($3s^2$), and Mn ($3p^64s^23d^5$) were treated as valence electrons, while projector augment wave (PAW) pseudopotential method was used to describe their interactions with cores.⁵ A default plane-wave cutoff energy was set to be 400 eV. The requested k-spacing was < 0.3 per angstrom, which leads to a $2 \times 2 \times 1$ mesh centered on the gamma point. The conjugate gradient approximation was employed, and the structures were relaxed. The formation energy (E_f) of different doping conditions was calculated by **equation S1**.⁶

$$E_f = E_d - E_p - \sum \mu_i \quad (\text{S1})$$

where E_d and E_p are the total energy of the doped and perfect crystal, respectively. μ_i is the is the chemical potential of atoms.

4. Equations



5. The Calculated Equations of EQE

The absorption efficiency (AE), internal quantum efficiency (IQE), and external quantum efficiency (EQE) are calculated by following equations:

$$AE = \frac{\int \lambda[E(\lambda) - R(\lambda)]d\lambda}{\int \lambda E(\lambda)d\lambda} \quad (\text{S7})$$

$$IQE = \frac{\int \lambda P(\lambda) d\lambda}{\int \lambda E(\lambda) d\lambda} \quad (\text{S8})$$

$$EQE = IQE \times AE = \frac{\int \lambda P(\lambda) d\lambda}{\int \lambda E(\lambda) d\lambda} \quad (\text{S9})$$

where $E(\lambda)/h\nu$, $R(\lambda)/h\nu$, and $P(\lambda)/h\nu$ are the number of photons in the excitation, reflectance, and emission spectra of the luminescent materials, respectively.

Table S1. EQE of single crystals and powder.

Sample	EQE of Powder (%)	EQE of Crystal (%)
$\text{K}_2\text{SiF}_6:\text{Mn}^{4+}$	67.50	78.20
$\text{Cs}_2\text{SiF}_6:\text{Mn}^{4+}$	37.90	63.20
$\text{Cs}_2\text{GeF}_6:\text{Mn}^{4+}$	37.70	66.90
$\text{Cs}_2\text{TiF}_6:\text{Mn}^{4+}$	32.20	52.80
$\text{Rb}_2\text{SiF}_6:\text{Mn}^{4+}$	55.80	80.20

Table S2. Crystal data and structure refinement for Rb₂NaAlF₆.

Empirical formula	Rb ₂ NaAlF ₆
Temperature	293(2) K
Crystal system, space group	Cubic, <i>Fm-3m</i>
Unit cell dimensions (Å)	$a = 8.291(2)$ $b = 8.291(2)$ $c = 8.291(2)$
Volume (Å ³)	570.0(4)
Z, Calculated density (g/cm ³)	4, 3.903
$F(000)$	608.0
Theta range for data collection(°)	4.257 – 24.491
Limiting indices	$-10 \leq h \leq 10, -10 \leq k \leq 10, -10 \leq l \leq 10$
Reflections collected / unique	1442 / 55 [$R(\text{int}) = 0.0473$]
Goodness-of-fit on F^2	0.978
Final R indices [$F_o^2 > 2\sigma(F_c^2)$] ^a	$R_1 = 0.0313, wR_2 = 0.0773$
R indices (all data) ^a	$R_1 = 0.00316, wR_2 = 0.0778$
Largest diff. peak and hole (e·Å ⁻³)	1.64 and -0.51

^a $R_1 = \Sigma||F_o| - |F_c||/\Sigma|F_o|$ and $wR_2 = [\Sigma w(F_o^2 - F_c^2)^2/\Sigma wF_o^4]^{1/2}$ for $F_o^2 > 2\sigma(F_o^2)$.

Table S3. Atomic coordinates ($\times 10^4$), equivalent isotropic displacement parameters ($\text{\AA}^2 \times 10^3$) and bond valence sum (BVS) calculations for $\text{Rb}_2\text{NaAlF}_6$. $U(\text{eq})$ is defined as one third of the trace of the orthogonalized U_{ij} tensor.

Atoms	x	y	z	$U(\text{eq})$	BVS
Rb(1)	7500	2500	7500	14.8(9)	1.44
Al(2)	5000	0	5000	4.4(13)	2.92
Na(3)	5000	5000	5000	12.7(18)	1.01
F(4)	5000	2184(07)	5000	13.7(9)	1.13

Table S4. Selected bond lengths (Å) and angles (°) for Rb₂NaAlF₆.

Rb(1)-F(4)	2.9431(9)	Al(2)-F(4)#12	1.811(6)
Rb(1)-F(4)#1	2.9431(9)	Al(2)-F(4)#13	1.811(6)
Rb(1)-F(4)#2	2.9431(9)	Al(2)-F(4)#14	1.811(6)
Rb(1)-F(4)#3	2.9431(9)	Al(2)-F(4)#10	1.811(6)
Rb(1)-F(4)#4	2.9431(9)	Al(2)-F(4)#1	1.811(6)
Rb(1)-F(4)#5	2.9431(9)	Al(2)-F(4)#	1.811(6)
Rb(1)-F(4)#6	2.9431(9)	Na(3)-F(4)#	2.335(6)
Rb(1)-F(4)#7	2.9431(9)	Na(3)-F(4)#15	2.335(6)
Rb(1)-F(4)#8	2.9431(9)	Na(3)-F(4)#11	2.335(6)
Rb(1)-F(4)#9	2.9431(9)	Na(3)-F(4)#2	2.335(6)
Rb(1)-F(4)#10	2.9431(9)	Na(3)-F(4)#16	2.335(6)
Rb(1)-F(4)#11	2.9431(9)	Na(3)-F(4)#17	2.335(6)
F(4)2-Rb(1)-F(4)#10	51.59(18)	F(4)#1-Al(2)-F(4)#12	90
F(4)#9-Rb(1)-F(4)#5	68.24(17)	F(4)#4-Al(2)-F(4)	90.000(1)
F(4)#6-Rb(1)-F(4)#8	119.739(11)	F(4)#16-Al(2)-F(4)	90
F(4)-Rb(1)-F(4)#9	119.738(11)	F(4)#1-Al(2)-F(4)	90.000(1)
F(4)#6-Rb(1)-F(4)#3	90.45(2)	F(4)#16-Al(2)-F(4)#12	90.000(1)
F(4)#9-Rb(1)-F(4)#2	90.453(19)	F(4)#16-Al(2)-F(4)#1	180
F(4)#6-Rb(1)-F(4)#2	119.739(11)	F(4)#16-Al(2)-F(4)#15	90.000(1)
F(4)#5-Rb(1)-F(4)#11	119.739(11)	F(4)#1-Al(2)-F(4)#15	90
F(4)#7-Rb(1)-F(4)#11	51.59(18)	F(4)#1-Al(2)-F(4)#4	90
F(4)#1-Rb(1)-F(4)#7	68.24(17)	F(4)#15-Al(2)-F(4)	90
F(4)#4-Rb(1)-F(4)#7	119.739(11)	F(4)#15-Al(2)-F(4)#12	90.000(1)
F(4)#9-Rb(1)-F(4)#10	119.739(11)	F(4)#12-Al(2)-F(4)	180
F(4)#5-Rb(1)-F(4)#10	51.59(18)	F(4)#4-Al(2)-F(4)#12	90
F(4)#5-Rb(1)-F(4)#7	90.45(2)	F(4)#16-Al(2)-F(4)#4	90
F(4)#2-Rb(1)-F(4)#7	119.739(11)	F(4)-Rb(1)-F(4)#2	119.739(11)
F(4)#9-Rb(1)-F(4)#3	51.59(18)	F(4)#7-Rb(1)-F(4)#8	169.8(2)
F(4)#11-Rb(1)-F(4)#3	68.24(17)	F(4)-Rb(1)-F(4)#4	51.59(18)
F(4)#9-Rb(1)-F(4)#8	51.59(18)	F(4)#4-Rb(1)-F(4)#2	68.24(17)
F(4)#1-Rb(1)-F(4)#6	119.739(11)	F(4)#4-Rb(1)-F(4)#3	90.45(2)
F(4)#10-Rb(1)-F(4)#3	169.8(2)	F(4)#4-Rb(1)-F(4)#6	169.8(2)
F(4)-Rb(1)-F(4)#8	90.45(2)	F(4)#4-Rb(1)-F(4)#8	68.24(17)
F(4)-Rb(1)-F(4)#11	68.24(17)	F(4)-Na(3)-F(4)#3	90.000(1)
F(4)#1-Rb(1)-F(4)#11	90.453(19)	F(4)#21-Na(3)-F(4)#3	90.000(1)

F(4)#4-Rb(1)-F(4)#11	119.739(11)	F(4)#11-Na(3)-F(4)#19	90.000(1)
F(4)#9-Rb(1)-F(4)#11	90.45(2)	F(4)#21-Na(3)-F(4)#20	90.000(1)
F(4)#1-Rb(1)-F(4)#9	169.8(2)	F(4)#3-Na(3)-F(4)#20	180
F(4)#6-Rb(1)-F(4)#11	51.59(18)	F(4)#11-Na(3)-F(4)#3	90
F(4)#5-Rb(1)-F(4)#2	51.59(18)	F(4)#3-Na(3)-F(4)#19	90.000(1)
F(4)#2-Rb(1)-F(4)#11	169.8(2)	F(4)#20-Na(3)-F(4)#19	90
F(4)#8-Rb(1)-F(4)#11	119.739(11)	F(4)-Na(3)-F(4)#11	90
F(4)-Rb(1)-F(4)#10	119.739(11)	F(4)#11-Na(3)-F(4)#21	180
F(4)#1-Rb(1)-F(4)#10	68.24(17)	F(4)-Na(3)-F(4)#19	180
F(4)#4-Rb(1)-F(4)#10	90.453(19)	F(4)-Na(3)-F(4)#20	90
F(4)#4-Rb(1)-F(4)#9	119.739(11)	F(4)#21-Na(3)-F(4)#19	90.000(1)
F(4)#1-Rb(1)-F(4)#4	51.59(18)	F(4)#11-Na(3)-F(4)#20	90
F(4)#6-Rb(1)-F(4)#10	90.45(2)	F(4)-Na(3)-F(4)#21	90.000(1)
F(4)#9-Rb(1)-F(4)#7	119.739(11)	F(4)#5-Rb(1)-F(4)#3	119.739(11)
F(4)#7-Rb(1)-F(4)#10	68.24(17)	F(4)#7-Rb(1)-F(4)#3	119.739(11)
F(4)#8-Rb(1)-F(4)#10	119.739(11)	F(4)#1-Rb(1)-F(4)#2	90.453(19)
F(4)#11-Rb(1)-F(4)#10	119.739(11)	F(4)#8-Rb(1)-F(4)#3	51.59(18)
F(4)-Rb(1)-F(4)#3	68.24(17)	F(4)#2-Rb(1)-F(4)#8	68.24(17)
F(4)-Rb(1)-F(4)#6	119.738(11)	F(4)#1-Rb(1)-F(4)#3	119.739(11)

Symmetry transformations used to generate equivalent atoms:

#1 $x+1, y, z$ #2 $-x+2, -y+1, -z+1$ #3 $x, y, z+1$
#4 $x+1/2, -y+1/2, z-1/2$ #5 $x-1, y, z$
#6 $x, y, z-1$ #7 $x-1/2, -y+1/2, z+1/2$
#1 $1/2+y, -1/2+z, +x$; #2 $1-y, 1/2-z, 3/2-x$; #3 $1-z, 1-x, 1-y$; #4 $+z, -1/2+x, 1/2+y$;
#5 $1/2+x, +y, 1/2+z$; #6 $1/2+z, +x, 1/2+y$; #7 $3/2-x, 1/2-y, 1-z$; #8 $1-x, 1/2-y, 3/2-z$;
#9 $1/2+y, +z, 1/2+x$; #10 $3/2-z, 1/2-x, 1-y$; #11 $1-y, 1-z, 1-x$; #12 $1-x, -y, 1-z$;
#13 $-1/2+x, -1/2+y, +z$; #14 $-1/2+x, +y, -1/2+z$; #15 $1-z, 1/2-x, 1/2-y$; #16 $1/2-y, 1/2-z, 1-x$;
#17 $-1/2+x, 1/2+y, +z$; #18 $3/2-x, 1-y, 3/2-z$; #19 $1-x, 1-y, 1-z$; #20 $+z, +x, +y$;
#21 $+y, +z, +x$

Table S5. ICP Results for the Mn Concentration of the 2 mol%Mn⁴⁺ RNAFM-P, the 2 mol%Mn⁴⁺ RNAFM-C and 2 mol%Mn⁴⁺, 10 mol%Mg²⁺ co-doped RNAFMM-C.

Sample	Theoretical Mn ⁴⁺ / Mg ²⁺ (mol%)	Experimental Mn ⁴⁺ / Mg ²⁺ (mol%)
2 mol%Mn ⁴⁺ RNAFM-P	2 / 0	0.9 / 0
2 mol%Mn ⁴⁺ RNAFM-C	2 / 0	1.1 / 0
2 mol%Mn ⁴⁺ , 10 mol%Mg ²⁺ co- doped RNAFMM-C	2 / 10	1.2 / 0.8

Table S6. The IQE, AE, and EQE of fluoride and oxyfluoride phosphors or non-equivalently doped with Mn⁴⁺.

Doping type	Phosphor matrix	IQE	AE	EQE	Reference
Heterovalent	K ₃ AlF ₆	88	57.5	50.6	7
	Rb ₃ AlF ₆	81.1	54	43.8	8
	Cs ₃ AlF ₆	48.2	/	/	9
	Na ₃ GaF ₆	69	/	/	10
	Na ₃ AlF ₆	69	/	/	10
	K ₃ GaF ₆	46	/	/	11
	K ₂ LiAlF ₆	87.5	/	15.7	12
	K ₂ NaAlF ₆	85	26	22.1	13
	Rb ₂ KAlF ₆	25.6	/	/	14
	Cs ₂ KAlF ₆	50.6	/	/	14
	Cs ₂ RbAlF ₆	33.8	/	/	14
	LiSrAlF ₆	78	/	/	15
	K ₂ NaGaF ₆	61.8	/	/	16
	Li ₃ Na ₃ Ga ₂ F ₁₂	81.2	15.4	12.5	17
	Li ₃ Na ₃ Al ₂ F ₁₂	28.7	47.1	13.5	17,18
	K ₃ ScF ₆	67.18	/	/	19
	K ₂ LiGaF ₆	20	/	/	20
	Cs ₂ KScF ₆	58.8	/	/	21
	K ₂ NaScF ₆	70.3	18.2	12.8	22
	Rb ₂ NaScF ₆	54.98	18.88	10.38	23
	Cs ₂ NaScF ₆	51.99	20.81	10.82	23
	K ₅ In ₃ F ₁₄	25.53	/		24
	Cs ₂ NaAlF ₆	37.2	59	21.95	25
	Cs ₂ NaGaF ₆ :Mn ⁴⁺ , Li ⁺	84.01	40	33.61	26
	K ₂ NaAlF ₆ :Mn ⁴⁺ , Mg ²⁺	65.4	60.5	39.6	27
	Rb ₂ NaAlF ₆	59.2			28
	K ₂ Li _{0.95} Na _{0.05} AlF ₆	8.5	/	/	29
	K ₂ Li _{0.9} Na _{0.1} AlF ₆	29.1	/	/	29
K ₂ Li _{0.8} Na _{0.2} AlF ₆	11.5	/	/	29	

$\text{K}_2\text{Li}_{0.7}\text{Na}_{0.3}\text{AlF}_6$	8.9	/	/	29
$[\text{C}(\text{NH}_2)_3]_3\text{AlF}_6$	27.8	23.1	6.4	30
K_2NbF_7	93.5	28.0	26.2	31
CsPF_6	55.7	90.6	50.4	32
RbPF_6	/	/	29.4	32
KPF_6	/	/	18.3	32
Na_2NbOF_5	67.6	25.4	17.17	33
$\text{K}_3\text{HF}_2\text{NbOF}_5$	73.28	49.68	36.4	34
$\text{Na}_2\text{WO}_2\text{F}_4$	76.64	/	/	35
$\text{K}_3\text{TaO}_2\text{F}_4$	23.4	/	/	36
$\text{BaNbF}_{5.5}(\text{OH})_{1.5}$	22	/	/	37
Cs_2NbOF_5	63.4	33.4	21.2	38
$\text{Cs}_2\text{MoO}_2\text{F}_4$	77.31	/	/	39
CsMoO_2F_3	54	/	/	40
$\text{Cs}_3\text{V}_2\text{O}_2\text{F}_7$	14	/	/	41
$(\text{NC}_4\text{H}_{12})_2\text{WO}_2\text{F}_4$	94.4	65.0	61.3	42
$(\text{NC}_4\text{H}_{12})_2\text{MoO}_2\text{F}_4$	89.3	64.0	57.1	42
$\text{Rb}_2\text{NaAlF}_6: \text{Mn}^{4+}, \text{Mg}^{2+}$	77.14	66.0	50.91	This work

Table S7. Doping Models and Formation Energy (E_f) of Mn^{4+} Doped and Mn^{4+} , Mg^{2+} Co-Doped RNAF.

Model	Substitution	Vacancy	E_d/eV	E_p/eV	E_f/eV
M1	Mn_{Al}		-396.70678	-396.1	4.5827
M2	Mn_{Al}^{\cdot}	V_{Rb}	-392.11616	-396.1	8.2386
M3	$Mn_{Al}^{\prime\prime}$	V_{Na}	-391.94377	-396.1	8.0476
M4	$Mn_{Al} + Mg_{Al}$		-392.31967	-396.1	6.7383

Table S8. Performance of the red LEDs based on RNAFM-P, RNAFM-C and RNAFMM-C at different forward currents, respectively.

Current (mA)	Samples	LE (lm/W)	T_c (K)
20	RNAFM-P	92.42	7273
20	RNAFM-C	104.26	6408
20	RNAFMM-C	118.48	7122
40	RNAFM-P	91.52	7425
40	RNAFM-C	102.63	6615
40	RNAFMM-C	117.35	7196
60	RNAFM-P	89.38	7598
60	RNAFM-C	99.21	6911
60	RNAFMM-C	114.29	7294
80	RNAFM-P	87.33	7765
80	RNAFM-C	95.92	7115
80	RNAFMM-C	112.56	7428
100	RNAFM-P	85.38	7925
100	RNAFM-C	93.70	7652
100	RNAFMM-C	108.96	7568
120	RNAFM-P	82.33	8138
120	RNAFM-C	90.66	8056
120	RNAFMM-C	107.24	7758
140	RNAFM-P	81.15	8292
140	RNAFM-C	87.97	8513
140	RNAFMM-C	104.25	7968

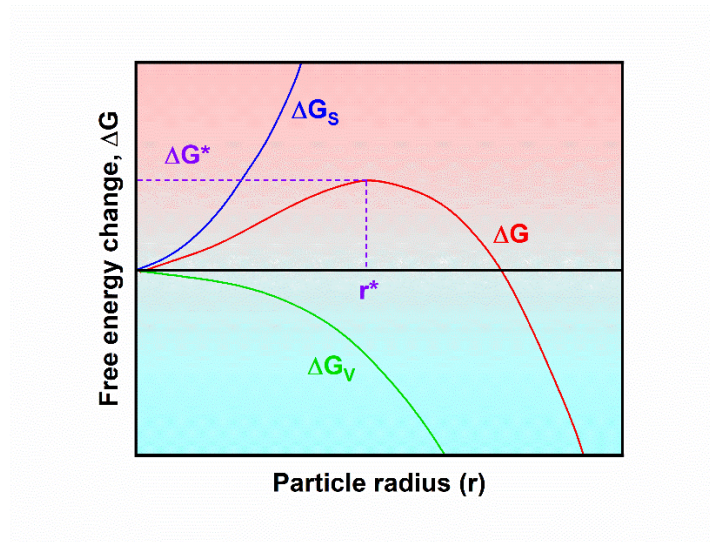


Figure S1. Schematic illustration of the Gibbs free energy change as a function of particle radius for homogeneous nucleation.

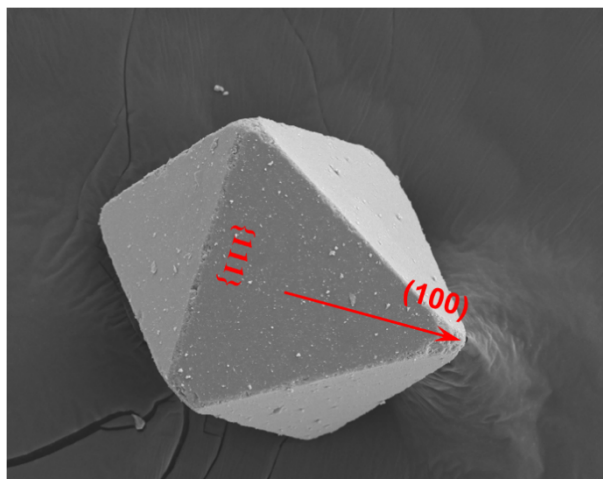


Figure S2. SEM image of a typical octahedron nanostructure with the $[001]$ zone direction and $\{111\}$ surfaces.

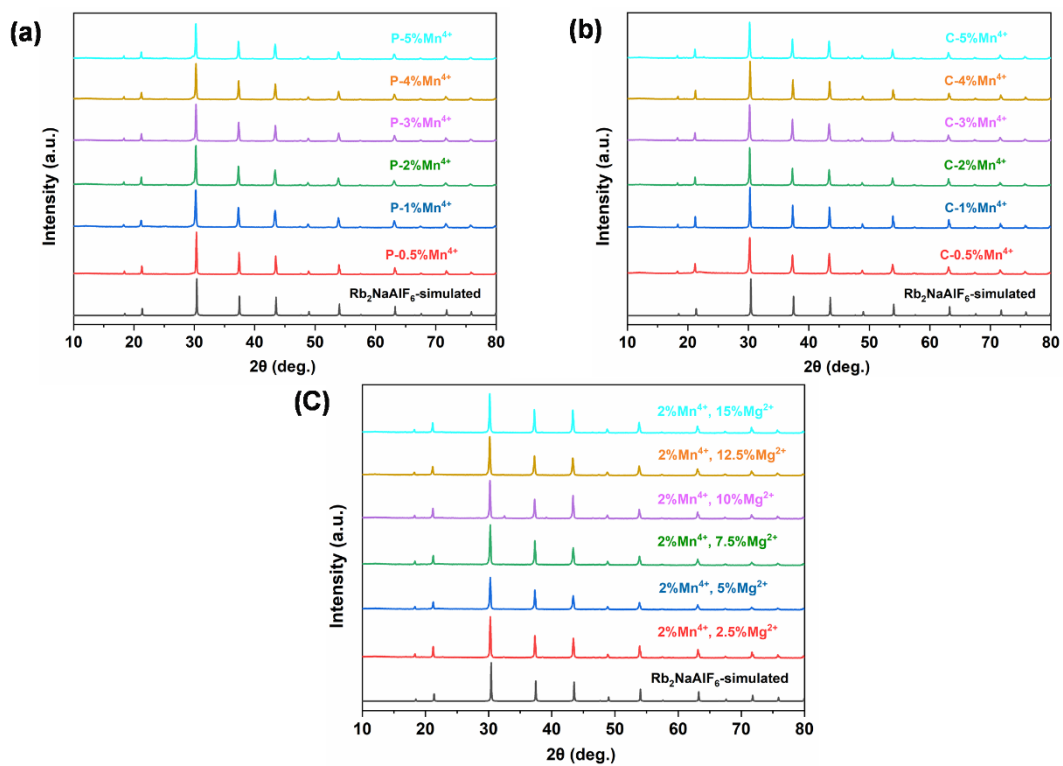


Figure S3. The XRD patterns of $\text{Rb}_2\text{NaAlF}_6$: Mn^{4+} powder samples of different Mn^{4+} doping.

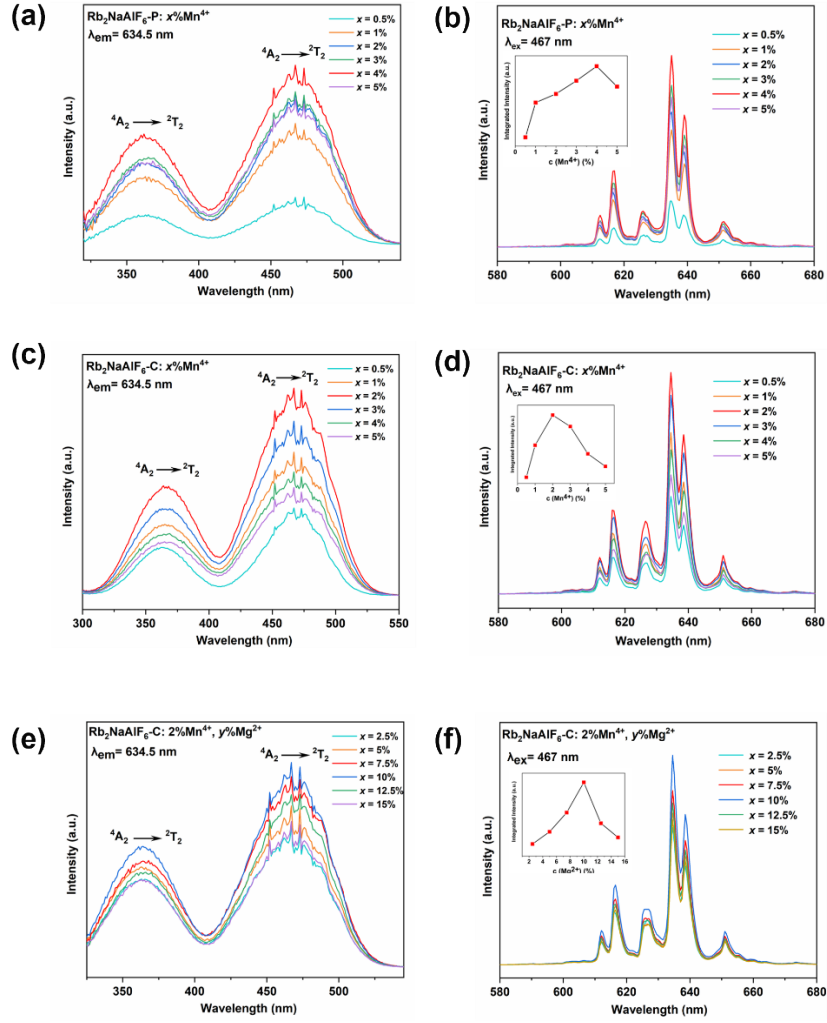


Figure S4. PLE (a) and PL (b) spectra of the $\text{Rb}_2\text{NaAlF}_6: \text{Mn}^{4+}$ powdery samples. PLE (c) and PL (d) spectra of the $\text{Rb}_2\text{NaAlF}_6: \text{Mn}^{4+}$ crystals. PLE (e) and PL (f) spectra of the $\text{Rb}_2\text{NaAlF}_6: 2\%\text{Mn}^{4+}, y\%\text{Mg}^{2+}$ crystals.

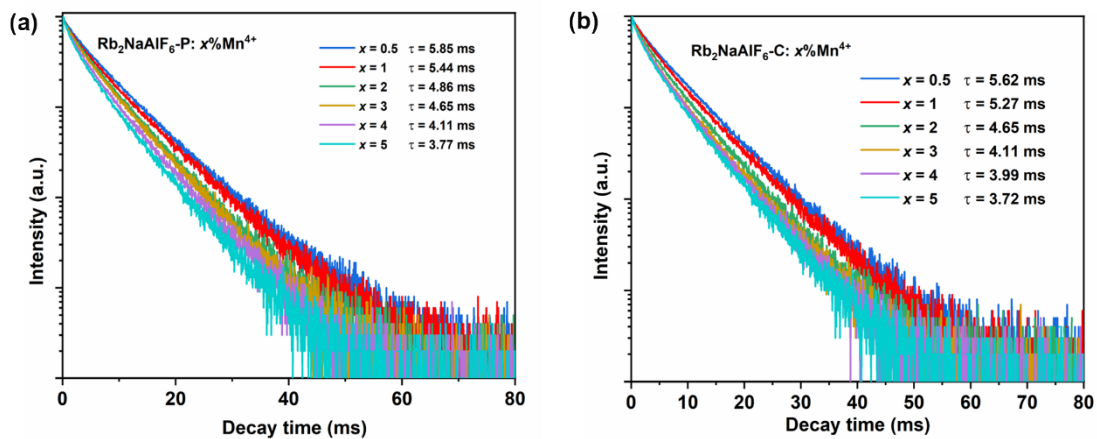


Figure S5. The room temperature concentration-dependent PL decay curves (a) the $\text{Rb}_2\text{NaAlF}_6: x\text{mol}\%\text{Mn}^{4+}$ powder phosphors, (b) the $\text{Rb}_2\text{NaAlF}_6: x\text{mol}\%\text{Mn}^{4+}$ crystals.

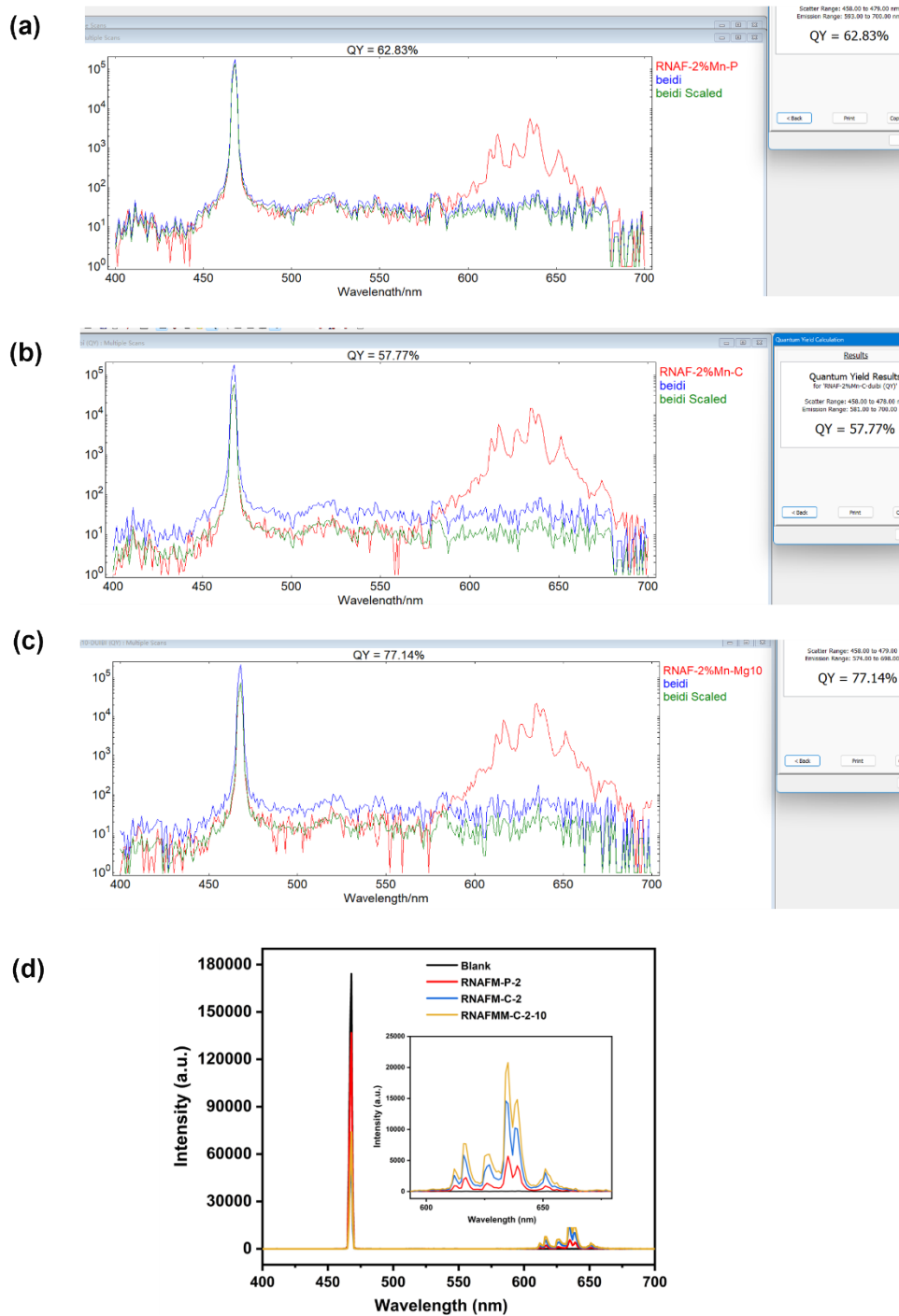


Figure S6. The original PLQY data of the $\text{Rb}_2\text{NaAlF}_6: x\%\text{Mn}^{4+}$ phosphors (a), the $\text{Rb}_2\text{NaAlF}_6: \text{Mn}^{4+}$ (b), the $\text{Rb}_2\text{NaAlF}_6: 2\%\text{Mn}^{4+}, 10\%\text{Mg}^{2+}$ (c), Calculated AE, IQE and EQE of the above three samples (d).

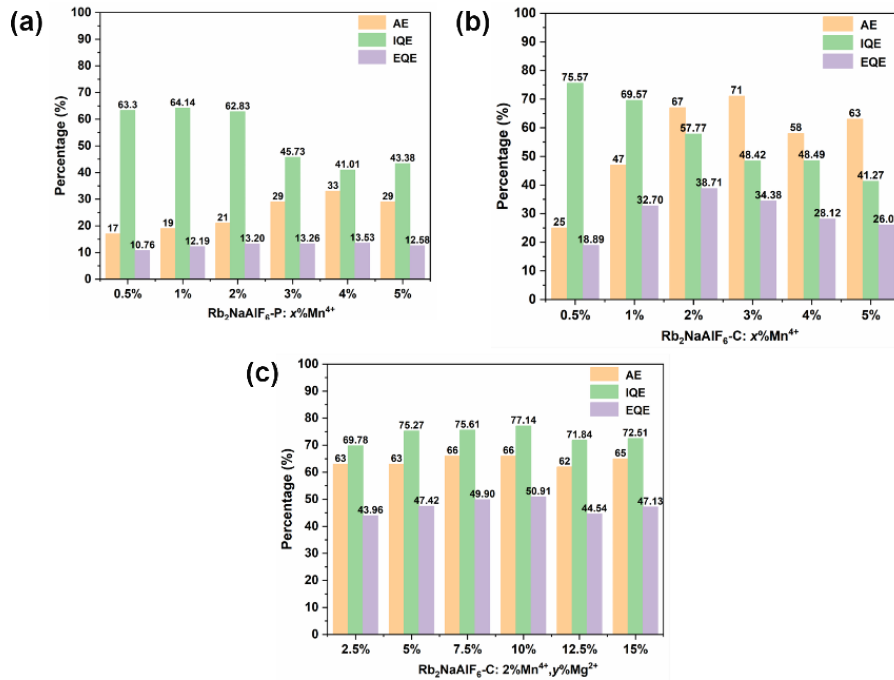


Figure S7. The QE of the different doping concentrations for Mn⁴⁺ for RNAFM-P (a), RNAFM-C (b) and Mn⁴⁺, Mg²⁺ co-doped RNAFM-C (c).

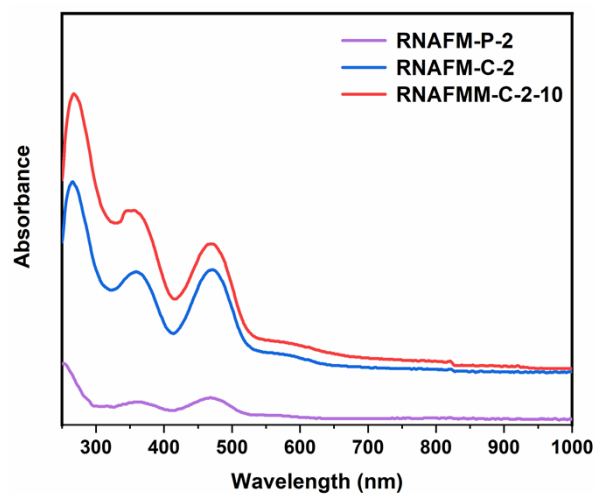


Figure S8. The absorbance spectra of the RNAFM-P-2, RNAFM-C-2 and RNAFMM-C.

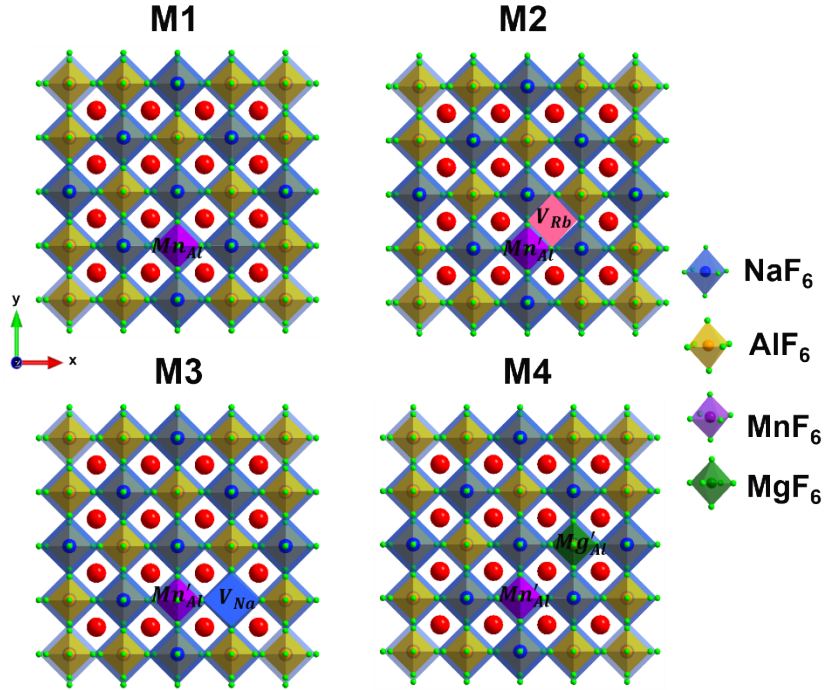


Figure S10. The possible structure of KNAF in $2 \times 2 \times 1$ supercell viewing along (001) direction. M1: Mn^{3+} substitutes the crystallographic position of Al^{3+} (Mn_{Al}). There is the valence state change of Mn^{4+} ; M2: A Mn^{4+} substitution of Al^{3+} in octahedral crystallographic position (Mn'_{Al}) and a 12 coordinated Rb^+ vacancy (V_{Rb}) defect to balance the valence state. M3: A Mn^{4+} substitution of Al^{3+} in octahedral crystallographic position (Mn'_{Al}) and a Na^+ vacancy (Mn'_{Na}) defect in octahedron position. M4: Mn^{4+} substitutes the crystallographic position of Al^{3+} , and Mg^{2+} substitutes Al^{3+} adjacent to Mn^{4+} , Mn'_{Al} and Mg'_{Al} form a valence equilibrium, and there is no vacancy defect in the theoretical structure.

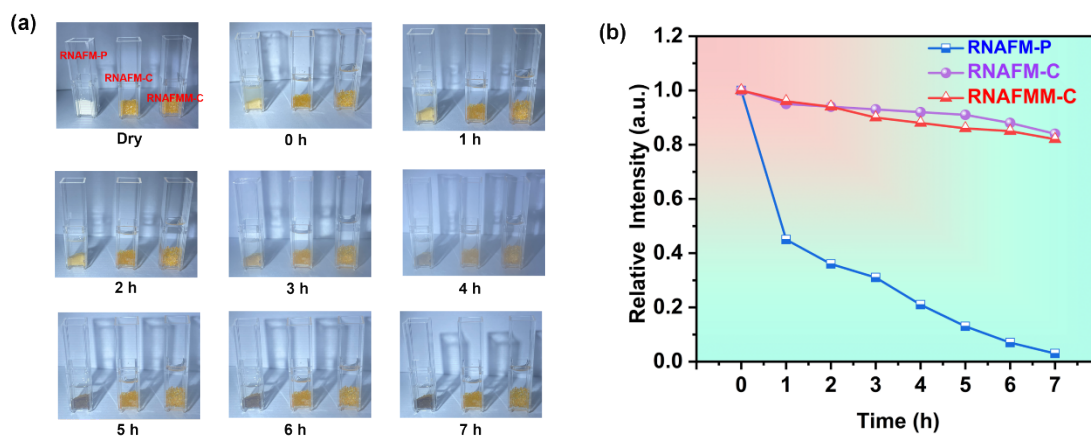


Figure S11. (a) The photographs of the RNAFM-P, RNAFM-C, and RNAFMM-C phosphors at high-temperature and high-humidity for 0-7 hours. (b) Relative PL intensity of the RNAFM-P, RNAFM-C, and RNAFMM-C at high-temperature and high-humidity for 0-7 hours.

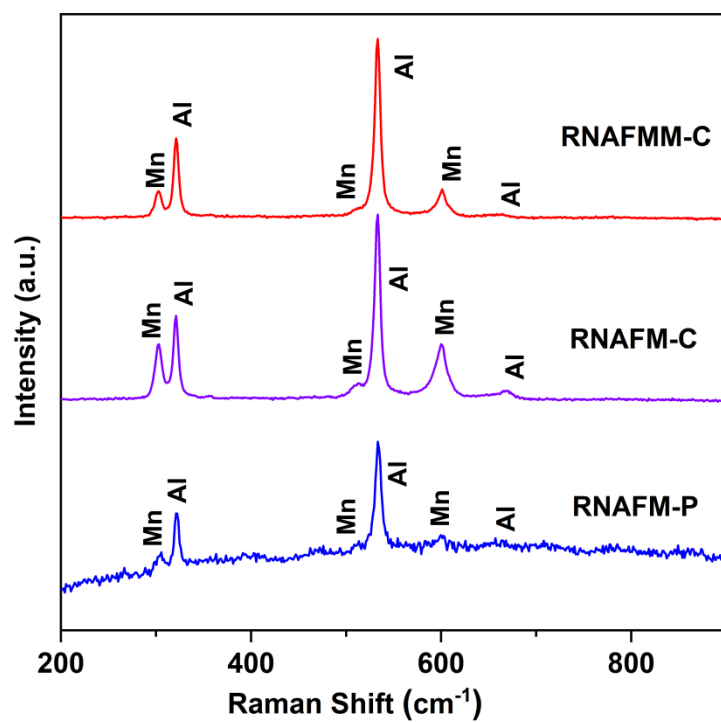


Figure S12. High resolution XPS spectra of the RNAFM-P, RNAFM-C, and RNAFMM-C phosphors.

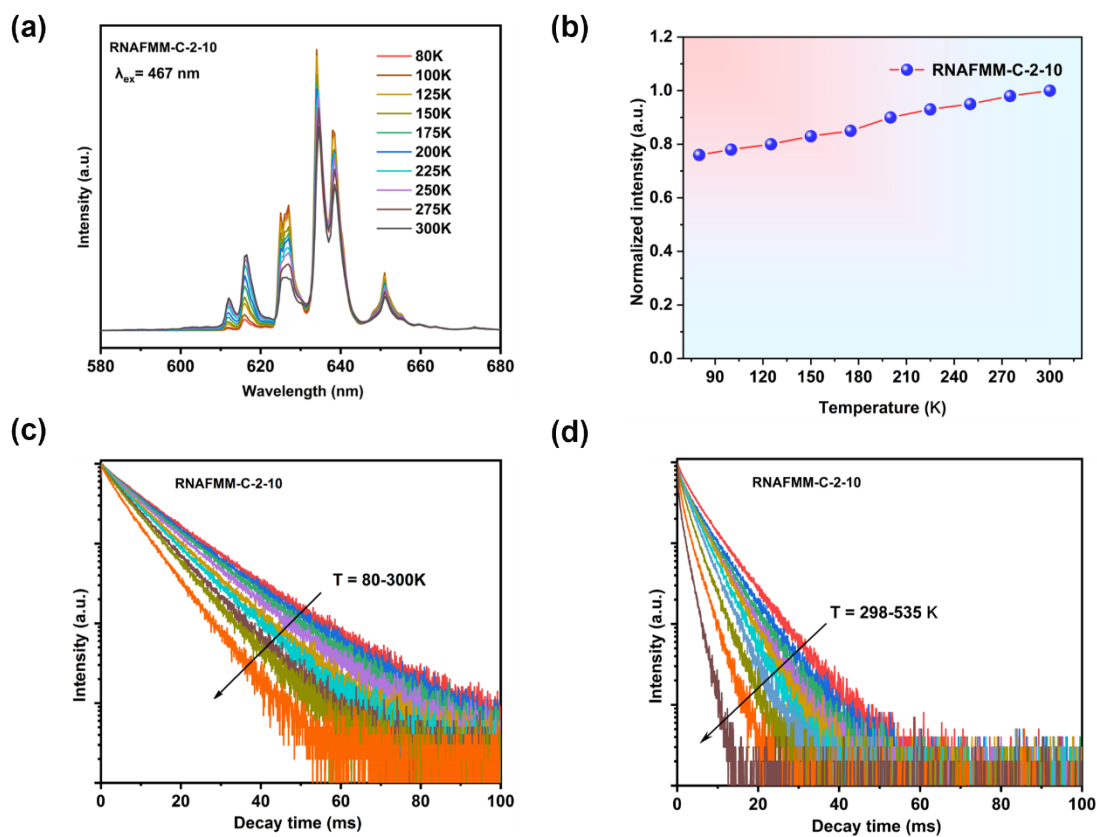


Figure S13. The temperature-dependent (a) PL spectra, (b) integrated PL intensity and (c) PL decay curves of RNAFMM-C crystals at a range of 80 to 300K. (d) The temperature-dependent PL decay curves of RNAFMM-C crystals at a range of 25 to 250°C.

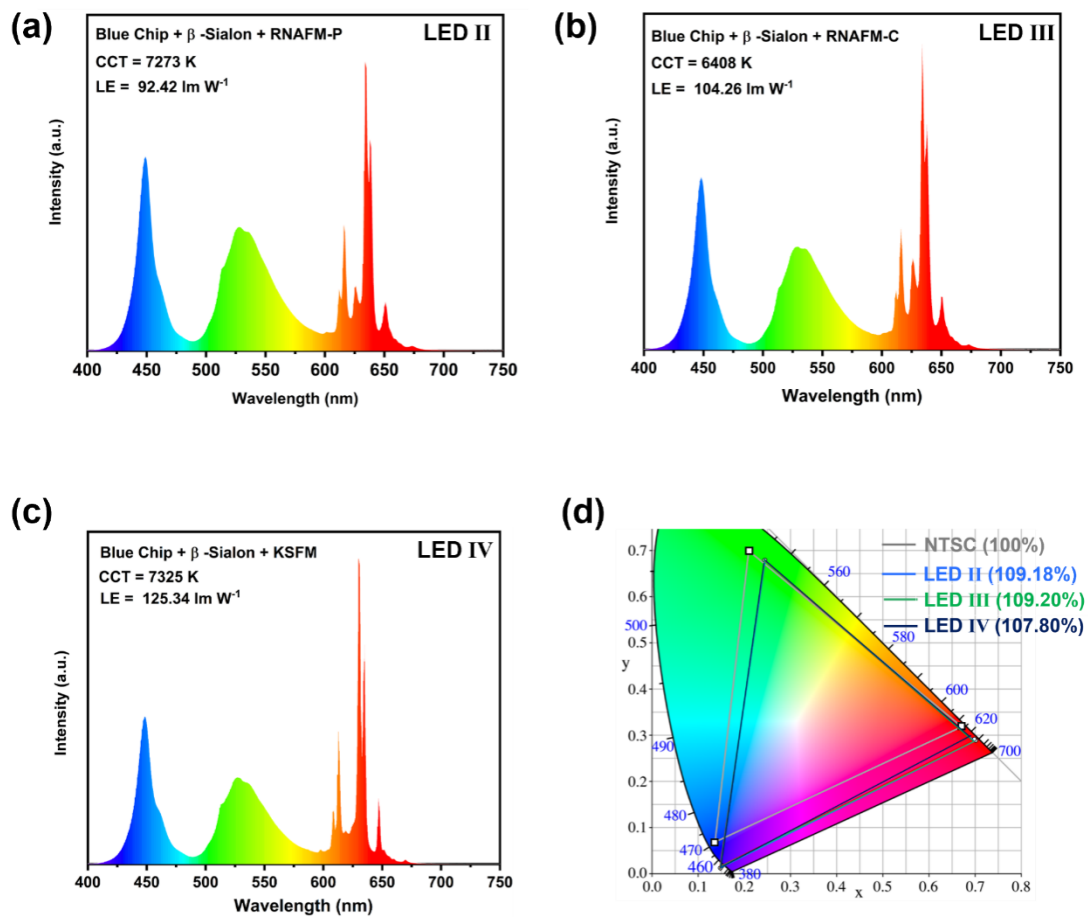


Figure S14. EL spectra of w-LEDs II-IV fabricated using (a) RNAFM-P, (b) RNAFM-C, and (c) KSFM after filtering. (d) CIE color gamut of w-LEDs and NTSC standard.

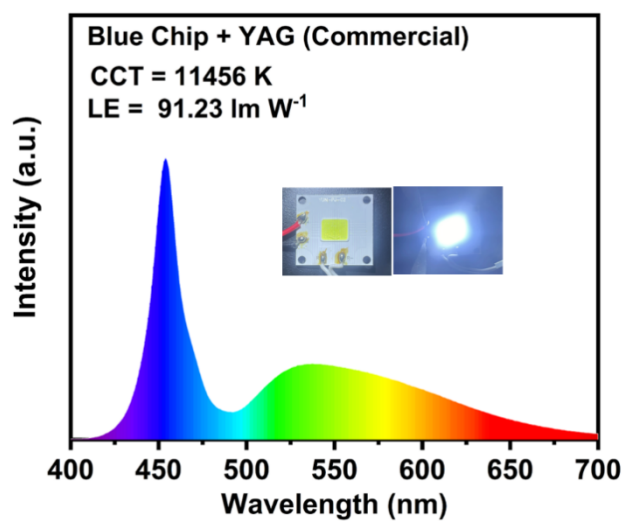


Figure S15. EL spectra of w-LED fabricated using commercial $\text{Y}_3\text{Al}_5\text{O}_{12}$ (YAG): Ce^{3+} phosphors.

REFERENCES

- [1] SAINT Plus, Version 7.60A; *Bruker Analytical X-ray Instruments*, **2000**.
- [2] G. M. Sheldrick, Crystal structure refinement with SHELXL. *Acta Crystallogr., Sect. C: Struct. Chem.* **2015**, *71*, 3.
- [3] J. P. Perdew, K. Burke, M. Ernzerhof, Generalized gradient approximation made simple, *Phys. Rev. Lett.* **1996**, *77*, 3865.
- [4] G. Kresse, J. Furthmüller, *Phys. Rev. B* **1996**, *54*, 11169.
- [5] G. Kresse, J. Furthmüller, *Comput. Mater. Sci.* **1996**, *6*, 15.
- [6] S. B. Zhang, S.-H. Wei, A. Zunger, *Phys. Rev. Lett.* **1997**, *78*, 4059.
- [7] E. Song, J. Wang, J. Shi, T. Deng, S. Ye, M. Peng, J. Wang, L. Wondraczek, Q. Zhang, *ACS Appl. Mater. Interfaces* **2017**, *9*, 8805.
- [8] T. Deng, E. Song, Y. Zhou, J. Yuan, *J. Alloys Compd.* **2019**, *795*, 453.
- [9] H. Ming, J. Zhang, L. Liu, J. Peng, F. Du, X. Ye, *ECS J. Solid State Sci. Technol.* **2018**, *7*, R149.
- [10] T. T. Deng, E. H. Song, J. Sun, L. Y. Wang, Y. Deng, S. Ye, J. Wang, Q. Y. Zhang, *J. Mater. Chem. C* **2017**, *5*, 2910.
- [11] T. T. Deng, E. H. Song, Y. Y. Zhou, L. Y. Wang, S. Ye, Q. Y. Zhang, *J. Mater. Chem. C* **2017**, *5*, 9588.
- [12] Y. Zhu, D. Chen, L. Huang, Y. Liu, M. G. Brik, J. Zhong, J. Wang, *J. Mater. Chem. C* **2018**, *6*, 3951.
- [13] X. Yi, R. Li, H. Zhu, J. Gao, W. You, Z. Gong, W. Guo, X. Chen, *J. Mater. Chem. C* **2018**, *6*, 2069.
- [14] T. T. Deng, E. H. Song, Y. Y. Zhou, L. Y. Wang, Q. Y. Zhang, *J. Mater. Chem. C* **2017**, *5*, 12422.
- [15] M. Zhu, Y. Pan, M. Wu, H. Lian, J. Lin, *J. Alloys Compd.* **2019**, *774*, 331.
- [16] S. Qiu, H. Wei, M. Wang, S. Zhang, Y. Zhou, L. Xu, X. Wang, H. Jiao, *RSC Adv.* **2017**, *7*, 50396.
- [17] M. Zhu, Y. Pan, Y. Huang, H. Lian, J. Lin, *J. Mater. Chem. C* **2018**, *6*, 491.
- [18] M. Zhu, Y. Pan, L. Xi, H. Lian, J. Lin, *J. Mater. Chem. C* **2017**, *5*, 10241.
- [19] H. Ming, S. Liu, L. Liu, J. Peng, J. Fu, F. Du, X. Ye, *ACS Appl. Mater. Interfaces* **2018**, *10*, 19783.
- [20] H. Cheng, Y. Song, F. Hong, G. Liu, D. Li, Q. Ma, X. Dong, J. Wang, W. Yu, *CrystEngComm* **2018**, *20*, 2183.
- [21] Y. Wang, C. Yu, Y. Zhou, E. Song, H. Ming, Q. Zhang, *J. Alloys Compd.* **2021**, *855*, 157347.
- [22] H. Ming, L. Liu, S. He, J. Peng, F. Du, J. Fu, F. Yang, X. Ye, *J. Mater. Chem. C* **2019**, *7*, 7237.
- [23] Y. Y. Zhou, E. H. Song, M. G. Brik, Y. J. Wang, T. Hu, Z. G. Xia, Q. Y. Zhang, *J. Mater. Chem. C* **2019**, *7*, 9203.
- [24] J. Yang, Q. Fan, J. Li, Y. Ye, Q. Zhou, Y. Zhou, Z. Wang, *Opt. Mater.* **2022**, *126*, 112223.
- [25] Y. Wang, W. Tang, C. Zhang, M. S. Molochev, H. Ming, Y. Zhou, S. Peng, E. Song, Q. Zhang, *Adv. Funct. Mater.* **2023**, *26*, 2313490.
- [26] W. Tang, Y. Wang, Y. Zhou, C. Zhang, Z. Chen, F. He, E. Song, Q. Zhang, *Adv. Optical Mater.* **2024**, *21*, 2400250.
- [27] Y. Wang, Y. Zhou, H. Ming, Y. Zhao, E. Song, Q. Zhang, *ACS Appl. Mater. Interfaces* **2021**, *13*, 51255.
- [28] D. Shi, Z. Liang, X. Zhang, Q. Zhou, Z. Wang, M. Wu, Y. Ye, *J. Lumin.* **2020**, *226*, 117491.
- [29] Y. Zhu, S. Yuan, L. Huang, Y. Liu, X. Li, J. Zhong, Y. Chen, D. Chen, J. Wang, *Dalton Trans.* **2019**, *48*, 711.

- [30] H. Ming, Y. Zhao, Y. Zhou, S. Zhang, Y. Wang, E. Song, Z. Xia, Q. Zhang, *ACS Appl. Electron. Mater.* **2020**, *2*, 4134.
- [31] H. Lin, T. Hu, Q. Huang, Y. Cheng, B. Wang, J. Xu, J. Wang, Y. Wang, *Laser Photonics Rev.* **2017**, *11*, 1700148.
- [32] Y. Chen, Z. Yang, Q. Wang, M. Rong, Q. Zhou, Z. Wang, *Dalton Trans.* **2019**, *48*, 10901.
- [33] K. Chen, Z. Shao, C. Zhang, S. Jia, T. Deng, R. Zhou, Y. Zhou, E. Song, *Chemical Engineering Journal* **2023**, *477*, 147165
- [34] L. Yao, S. He, W. Nie, L. Fu, Z. Liao, W. Cai, R. Wang, J. Peng, X. Ye, *J. Lumin.* **2021**, *238*, 118315.
- [35] T. Hu, H. Lin, Y. Cheng, Q. Huang, J. Xu, Y. Gao, J. Wang, Y. Wang, *J. Mater. Chem. C* **2017**, *5*, 10524.
- [36] Y. Zhou, S. Zhang, X. Wang, H. Jiao, *Inorg. Chem.* **2019**, *58*, 4412.
- [37] Z. Yang, Q. Wei, N. Wang, Z. Yang, Q. Zhou, Z. Wang, H. Liang, *ECS J. Solid State Sci. Technol.* **2017**, *6*, R139.
- [38] H. Ming, J. Zhang, L. Liu, J. Peng, F. Du, X. Ye, Y. Yang, H. Nie, *Dalton Trans.* **2018**, *47*, 16048.
- [39] S. He, L. Yao, W. Cai, D. Wu, J. Peng, X. Ye, *Dalton Trans.* **2020**, *49*, 11290.
- [40] S. He, F. Xu, T. Han, Z. Lu, W. Wang, J. Peng, F. Du, F. Yang, X. Ye, *Chem. Eng. J.* **2020**, *392*, 123657.
- [41] X. Yang, C. Liao, Z. Jin, Q. Wang, W. Xie, P. Yang, Z. Wang, *Mater. Res. Bull.* **2022**, *150*, 111798.
- [42] H. Ming, Y. Zhao, Y. Zhou, M. S. Molokeev, Y. Wang, E. Song, Q. Zhang, *Adv. Optical Mater.* **2023**, *11*, 2300076.